HOKKAIDO UNIVERSITY

Title	Interaction of the Halobacterial Transducer to a Halorhodopsin Mutant Engineered so as to Bind the Transducer : Cl- Circulation within the Extracellular Channel
Author(s)	Hasegawa, Chisa; Kikukawa, Takashi; Miyauchi, Seiji et al.
Citation	Photochemistry and Photobiology, 83(2), 293-302 https://doi.org/10.1562/2006-06-09-RA-916
Issue Date	2007-03
Doc URL	https://hdl.handle.net/2115/33763
Rights	Author Posting. © The Authors 2007 This is the author's version of the work. It is posted here for personal use, not for redistribution. The definitive version was published in Photochemistry and Photobiology, Volume 83, Issue 2, Page 293-302. http://dx.doi.org/10.1562/2006-06-09-RA-916
Type	journal article
File Information	PP83-2I.pdf

Hokkaido University Collection of Scholarly and Academic Papers : HUSCAP

Interaction of the Halobacterial Transducer to a Halorhodopsin Mutant Engineered so as to Bind the Transducer: Cl^- Circulation within the Extracellular Channel

Chisa Hasegawa[#1], Takashi Kikukawa[#2], Seiji Miyauchi[1], Akiteru Seki[1], Yuki Sudo[1], Megumi Kubo[3], Makoto Demura[3] and Naoki Kamo*[1]

[1]Laboratory of Biophysical Chemistry, Graduate School of Pharmaceutical Sciences, Hokkaido University, Sapporo, Japan

[2]Laboratory of Biomolecular Systems, Creative Research Initiative "Sosei" (CRIS), Hokkaido University, Sapporo, Japan

[3]Department of Biomolecular Science, Faculty of Advanced Life Science, Hokkaido University, Sapporo, Japan

Laboratory of Biophysical Chemistry, Graduate School of Pharmaceutical Sciences, Hokkaido University, N12W6, Sapporo 060-0812, Japan

Phone: +81-11-706-3923

Fax: +81-11-706-4984

e-mail: nkamo@pharm.hokudai.ac.jp

Abbreviations: bR, bacteriorhodopsin; cRNA, complementary RNA; CP, cytoplasmic; DDM, n-dodecyl-β-D-maltoside; EC, extracellular; hR, halorhodopsin; HtrI, halobacterial transducer of sR; HtrII, halobacterial transducer of pR; MCP, methyl-accepting chemo-taxis protein; *p*hR, halorhodopsin from *Natronomonas pharaonis*; *p*HtrII, HtrII from *Natronomonas pharaonis*; *p*HtrII$^{1-159}$, N-terminal sequence of 159 amino acid residues of *p*HtrII; *pp*R, phoborhodopsin from *Natronomonas pharaonis*; pR, phoborhodopsin; *s*hR, halorhodopsin from *Halobacterium salinarum*; sR, sensory rhodopsin.

[#]These two authors contributed equally to this work.

*To whom correspondence should be addressed.

ABSTRACT

An alkali-halophilic archaeum, *Natronomonas pharaonis*, contains two rhodopsins that are halorhodopsin (*p*hR), a light-driven inward Cl^- pump and phoborhodopsin (*pp*R), the receptor of negative phototaxis functioning by forming a signaling complexes with a transducer, *p*HtrII. Previously, we reported that the *p*hR double mutant, P240T/F250Y^{phR}, can bind with *p*HtrII [Y. Sudo *et al*. (2006) *J. Mol. Biol*. **357**, 1274-1282]. This mutant itself can transport Cl^-, while the net transport was stopped upon formation of the complex. The flash photolysis data were analyzed by a scheme in which *p*hR $\Rightarrow$ $P_1 \rightarrow P_2 \rightarrow P_3 \rightarrow P_4 \rightarrow$ *p*hR. The P_3 of the wild-type and the double mutant contained two components, X- and O-intermediates. After the complex formation, however, the P_3 of the double mutant lacked the X-intermediate. These observations imply that the X-intermediate (probably the N-intermediate) is the state having Cl^- in the cytoplasmic binding site and that the complex undergoes an extracellular

Cl^- circulation due to the inhibition of formation of the X-intermediate.

INTRODUCTION

Halorhodopsin (hR) is a light-driven inward Cl^- pump expressed in the membrane of halobacterium and was originally found in *Halobacterium salinarum*, halophilic archaea (1-3). Halorhodopsin is a colored membrane protein whose absorption maximum is located at 578 nm. This protein has all-*trans* retinal as a chromophore as is true of other archaeal rhodopsins such as bacteriorhodopsin (bR)(4,5), sensory rhodopsin (sR; also called sensory rhodopsin I, SRI)(6,7) and phoborhodopsin (pR; also called sensory rhodopsin II, SRII)(8-11). These archaeal rhodopsins have the same global fold, and the chromophore binds to a conserved lysine residue on the seventh helix (G-helix) via a protonated Schiff base.

Out of four kinds of archaeal rhodopsins, two, bR and hR, function as a light-driven ion pump, while the other two function as a photoreceptor. sR (or SRI) acts as a receptor of the positive and negative photo-taxis (6): the ground state of sR whose absorption maximum is located around 590 nm is

a receptor of the positive photo-taxis, while its long-life photo-intermediate absorbing 373 nm light is a receptor of the negative phototaxis. On the other hand, pR (or SRII) is a receptor of negative photo-taxis, and its absorption maximum is located around 500 nm (8-11). Thus, the archaea are attracted to long-wavelength light (λ > 520 nm) where they obtain solar energy via bR and hR whose λ_{max}'s are located at 570 – 580 nm. On the other hand, the archaea show avoidance of short-wavelength light (λ < 520 nm) containing dangerous UV light.

These photoreceptors form 2:2 complexes in the membrane with the respective cognate transducer proteins, HtrI (for sR or SRI) and HtrII (for pR or SRII) (12-14). These complexes transmit the light signal to a cytoplasmic part of the transducer to activate the phosphorylation cascades that modulate the flagella motors (15). The transducer (HtrI or HtrII) is a two-transmembrane helical protein that belongs to a family of methyl-accepting chemo-taxis proteins

(MCPs)(16,17). MCP exists as a homo-dimer composed of a 50-60 kDa subunit and forms a ternary complex with CheA and CheW.

How do the photoreceptor and the transducer form the signaling complex? The X-ray crystallographic structure of the complex between *pp*R and *p*HtrII reveals the formation of three hydrogen bonds whose pairs are $Tyr199^{ppR}$/$Asn74^{pHtrII}$ and $Thr189^{ppR}$/$Glu43^{pHtrII}$/$Ser62^{pHtrII}$ (18), where *pp*R and *p*HtrII are, respectively, *pharaonis* phoborhodopsin (also called *Np*SRII) and *pharaonis* halobacterial transducer II, which are both derived from *Natronomonas pharaonis*. The importance of these hydrogen bonds to the binding has been proved experimentally (19). Interestingly, bR and hR that originally cannot bind with *p*HtrII become able to bind when hydrogen bond-forming amino acid residues are introduced at their proper positions.

In this paper, we examined the Cl^- transport activity and photocycle of the complex between a truncated *p*HtrII (*p*$HtrII^{1-159}$, an N-terminal sequence of 159 amino acid residues) and a *p*hR (halorhodopsin from *N. pharaonis*) mutant in which the hydrogen bond-forming amino acid residues are introduced.

We observed that 1) the complex formation blocks the Cl^--pumping of *p*hR(P240T/F250Y) and 2) a certain photo-intermediate (called tentatively X) is not observed after the complex formation during the photocycle. We will discuss the possible mechanism of the Cl^--transport of hR.

MATERIALS AND METHODS

Protein expression and purification. The constructions of expression plasmids for C-terminal His-tagged wild-type *p*hR and *p*HtrII$^{1-159}$ were reported previously (19-21). The plasmids for the *p*hR mutants were prepared with a Quikchange site-directed mutagenesis kit (Stratagene Cloning Systems, San Diego, CA). The proteins were prepared as described (20,21). Briefly, these proteins were expressed in *E. coli* BL21(DE3) cells, solubilized with 1.5% n-dodecyl-β-D-maltoside (DDM) and purified by a Ni-NTA agarose column and a subsequent gel filtration column. The samples were then concentrated by ultrafiltration (if necessary) and dialyzed against the appropriate buffer

solutions.

Denaturation kinetics of phR mutants. The thermal stability of the *p*hR mutants was examined as described previously (22). The residual *p*hR amounts after incubation at high temperatures (60 or 70°C) were estimated from the absorbance at 578 nm using a Model V-560 spectrophotometer (Jasco, Tokyo, Japan).

Protein expressions in Xenopus oocytes. For *in vitro* synthesis of complementary RNA (cRNA), the genes encoding wild-type *p*hR, the P240T/F250Y^{phR} mutant and *p*HtrII$^{1-159}$ were cloned into the pGH19 plasmid. The target genes including C-terminal His-tags were amplified by PCR using the plasmid DNAs for their expressions in *E. coli* cells as templates. The PCR was carried out using two overlapping primers introducing 3'-*Hind*III restriction sites. The amplified DNA fragments were sub-cloned into pGEM-T vector (Promega), and the DNA sequences were confirmed using a standard procedure (377 DNA

sequencer, Applied Biosystems, Foster City, CA). The obtained plasmids were restricted, and the resultant DNA fragments were ligated to the *Eco*RI and *Hind*III sites of the pGH19 plasmid. The resultant product was partially sequenced to confirm the orientation of the insert. Capped cRNAs were synthesized from the obtained pGH19 plasmids using a mMESSAGE mMACHINE kit (Ambion, Inc., Austin, TX).

The isolation of *Xenopus* oocytes was performed as described previously (23). For the expression of the wild-type *p*hR and its double mutant P240T/F250Y^{phR}, 50 ng of the cRNAs were injected. For the co-expressions of P240T/F250Y^{phR} and *p*HtrII$^{1-159}$, 30 ng of P240T/F250Y^{phR} and 0-10 ng of *p*HtrII$^{1-159}$ cRNAs were injected. The oocytes were incubated for 3-5 days at 18°C in the presence of 1-3 μM all-*trans* retinal.

The relative expression amounts of the proteins were evaluated using the antibody against His-tags fused to their C-terminuses. The oocytes expressing the target proteins were homogenized and then centrifuged at 1,000 x g for 10 min.

The membrane fraction was collected from the supernatant after further centrifugation at 10,000 x g for 20 min. The obtained membrane fractions were analyzed by the Western blot according to a standard procedure.

Photo-induced current measurements. The electrophysiological recordings were performed as described previously (23). The potential of the oocyte membrane was clamped at -50 mV using the two-electrode voltage clamp technique. The perfusion buffer was 10 mM Hepes, pH 7.4, including 96 mM NaCl, 2 mM KCl, 1.8 mM $CaCl_2$ and 1 mM $MgCl_2$. The photo-induced current was calculated as the difference in the steady state current before and after irradiation with a green light (530 ± 18 nm).

Flash photolysis spectroscopy. All measurements were performed at 20°C, and the absorbance values of the samples were 0.5-1.0 at 580 nm. The buffer solution used was 10 mM Mops, pH 7.0, including 0.1% DDM and various concentrations

of NaCl. For the photocycle measurements of P240T/F250Y^{phR} bound with *p*HtrII$^{1-159}$, they were mixed so that at least 90% of P240T/F250Y^{phR} forms the complex within the sample cell. Here, the amount of *p*HtrII$^{1-159}$ necessary for >90 % formation was calculated using the previously reported dissociation constant, 29.1 μM, between P240T/F250Y^{phR} and *p*HtrII$^{1-159}$ (19).

The details of the flash-photolysis apparatus and the procedure for data analysis were reported previously (21). The transient absorption changes induced by a laser pulse (Nd:YAG, 532 nm, 7 ns, 5 mJ/pulse) were acquired in a computer at every 0.5 μs between -44 and 220 ms. The data before the laser pulse (-44 - 0 ms) were adopted as a baseline for the calculation of the following absorption change. At each selected measuring wavelength (every 10 nm from 410 to 710 nm), 50 - 100 laser pulses were used to improve the S/N ratio. The data points were then selected by choosing a logarithmic time scale to reduce the number of points. The scattered laser pulse caused a strong artifact. At 530 nm, the artifact continued up to 25 μs. For the following fitting analysis,

thus, the data at 30 wavelengths except for 530 nm were adopted. Those data after 10 μs were fitted.

The method of analysis was based on that of Chizhov *et al*. (24,25). The obtained data were fitted simultaneously with the multi-exponential function using the Origin (OriginLab, Northampton, MA) and Igor Pro(WaveMetrics, Lake Oswego, OR). The data weight was determined independently for each wavelength by estimating the average error from the baseline part (-44 to 0 ms). For each data set, the fittings were performed using 3-5 exponential functions. In all data sets, the reductions in the standard deviation of the weighted residuals were saturated at a 4-exponential function. Thus, the further analysis was performed according to the following sequential model: $P_0 \Rightarrow P_1 \rightarrow P_2 \rightarrow P_3 \rightarrow P_4 \rightarrow P_0$, where P_0 means the unphotolyzed original state, and P_i (i=1-4) means the photochemically defined state that may contain a few physically defined intermediates in some cases. By using the fitting results at a 4-exponential function, the time constants τ_i and the absorption differences between P_i and P_0

($\Delta\varepsilon_i$) were calculated. Independently, we fitted the measured absorption spectrum of the unphotolyzed state (250-750 nm) with the sum of three skewed Gaussian functions and the terms expressing background scattering ($A + B/\lambda^4$; λ in nm). The skewed Gaussian function is defined by the four parameters: λ_{max} (in nm), A_{max} (amplitude at λ_{max}), ρ (skewness of the absorption band) and $\Delta\nu$ (half-bandwidth in cm^{-1}) (24). For the spectrum of the unphotolyzed state, the three skewed Gaussian functions correspond with the main absorption band around 580 nm, the β-band around 400 nm and the band due to aromatic amino acid residues around 280 nm, respectively, and the sum of the first two expresses the retinal spectrum in the P_0 state. By adding the retinal spectrum of the P_0 state to the absorption differences ($\Delta\varepsilon_i$), we finally obtained the absolute spectra of the P_i states. For further details, see previous reports (21,24,25).

RESULTS

A *p*hR mutant that is able to bind with *p*HtrII

A previous report has showed that a *p*hR double mutant, P240T/F250Y^{phR} can bind to *p*HtrII$^{1-159}$ with a dissociation constant of 29.1 μM, which was proved by isothermal titration calorimetry (19). Here, we examined the binding using another method; when *pp*R or its mutants can form a complex with *p*HtrII$^{1-159}$, the thermal stability of the complex increases in comparison with the pigment alone, which is easily observable by measuring the denaturation rate at high temperature (22). Figures 1 A and B show the denaturation rates of the single mutants of P240T^{phR} and F250Y^{phR}, indicating no or weak interactions between these mutants and the *p*HtrII$^{1-159}$. Even at a large molar ratio of *p*HtrII$^{1-159}$, no essential changes in their thermal stabilities were observed. Figure 1 C clearly shows the increase in the thermal stability of the double mutant P240T/F250Y^{phR} in the presence of *p*HtrII$^{1-159}$.

Figure 1 also shows that the simultaneous mutations, P240T/F250Y, make the protein unstable. These residues face the outside of the protein, and so the displacements by the hydrophilic residues may alter the interaction with the solvent and/or the detergent. This instability was measurable only at high temperature (60°C). During the photo-electric current and the flash-photolysis experiments performed below 25°C, the denaturation of the double mutant was negligible.

Photo-electric current through *Xenopus* oocyte membrane co-expressing the *p*hR mutant and *p*HtrII$^{1-159}$

Electrophysiological methods using *Xenopus* oocyte expression system have been proven to be useful for investigation of ion-channels and electrogenic transporters. bR, channelrhodopsin and *pp*R have been investigated using this method, and the results obtained provided valuable insight (26-29). Figure 2 shows the photo-induced electrical current

through the oocyte membrane expressing *p*hR in the presence or absence of *p*HtII$^{1-159}$. Here, we present the currents measured with a perfusion buffer including about 100 mM Cl^-. With the increasing Cl^- concentration, the current increased and became almost saturated at 100 mM Cl^- (data not shown). The left histogram in Fig. 2 A represents the amount of current *via* wild-type *p*hR. Bamberg and coworkers observed the photo-induced current by bR expressing in the oocyte membrane, and the current in this experiment is much larger than that of bR (26).

The right histogram in Fig. 2 A represents the electrical current by the double mutant of *p*hR, P240T/F250Y^{phR}. The amount of expressed proteins evaluated by the Western blot was about half that of the wild-type (lanes 1 and 2 in Fig. 2 C) Thus, the relative pumping activity of the double mutant is estimated to be about a quarter of that of the wild-type. Because these two mutated residues are pointed to the outside of *p*hR, the direct interaction of these residues with the transporting Cl^- ion might not be probable; thus, we do not

know the reason for the weak pumping activity of the double mutant at present.

Figure 2 B represents the effect of *p*HtrII on the *p*hR pumping activity. The injected cRNA of P240T/F250Y^{phR} was kept at 30 ng, while that of *p*HtrII$^{1-159}$ was varied from 0 to 10 ng. The molar ratios of actually expressed proteins were approximately 1:0, 1:0.4, 1:1.8, 1:3.9 from left to right, which were estimated from the bands of lanes 3-6 in Fig. 2 C. The expressed amounts of P240T/F250Y^{phR} were not essentially affected by the co-expression of *p*HtrII$^{1-159}$. These results clearly reveal that the pumping activity of the double mutant decreases with an increase in the molar ratio of *p*HtrII$^{1-159}$.

Complete blocking of the Cl^--pumping activity was not observed, however. On the other hand, the co-expression of *pp*R (F86D^{ppR}; due to a larger photo-current than the wild-type) and *p*HtrII$^{1-159}$ in the oocyte blocks nearly completely except for the transient signal observed immediately after the illumination is applied (30). One of possible reasons for the

incomplete blocking is the large dissociation constant, K_D; the K_D for the binding of the wild-type *p*pR and *p*HtrII$^{1-159}$ is 0.16 µM in 0.05% DDM, while that of the *p*hR double mutant is 29.1 µM in the same detergent (19), meaning that the binding of the *p*hR mutant with *p*HtrII$^{1-159}$ is approximately 180-fold weaker than that of *p*pR. Another point to be considered is the concentrations of these proteins in the oocyte membrane, which may not be estimated, however. Although within the membrane, the binding might become stronger than in the solution with detergent, it is probable that the protein concentrations may be too small for complete binding. Therefore, we conclude that the complex between *p*hR and *p*HtrII abolishes the pumping activity. The same conclusions have been drawn for sR (SRI) and *p*pR (NpSRII) (31,32).

Another difference in the photocurrent between *p*pR and *p*hR is the initial transient signal reported in *p*pR (NpSRII) mentioned above (30). For the present *p*hR experiments, no such initial transient signals were observed. It is noted that in the present experiments, the recording of signals was

done with a pen-writing recorder that has a slow response, and such transient signals might be ignored. Further studies are necessary and the origin of these transient signals (if they exist) is the next aim of the investigation.

Flash-photolysis studies

Flash-photolysis experiments were performed for the purified wild-type *p*hR, P240T/F250Y^{phR} and its complex with *p*HtrII$^{1-159}$ in the presence of various concentrations of Cl^-. These three proteins were prepared independently from the *E. coli* membranes. For a sample of the complex, the purified P240T/F250Y^{phR} and *p*HtrII$^{1-159}$ were mixed so that more than 90% of P240T/F250Y^{phR} forms the complex (see MATERIALS AND METHODS). Figure 3 shows the transient absorption changes at three selected wavelengths that are representative of the formation and decay of L (500 nm) and O (650 nm) intermediates and the depletion and recovery of the initial unphotolyzed state (580 nm). All samples showed essentially the same photocycle in

terms of the appearance of the representative intermediates, L and O. However, remarkable differences are seen in the 650 nm decay: a prolonged decay appeared upon complex formation at 0.2 M Cl^- (right upper panel). Moreover, the difference in the accumulation of the O-intermediate is also notable. For wild-type *p*hR, the accumulation of the O-intermediate decreases at a high concentration of 4.0 M Cl^- (lower left panel). This decrease is moderate for P240T/F250Y^{phR} (lower middle panel) and the complex (lower right panel).

The transient absorption changes at wavelengths from 410 to 710 nm (every 10-nm interval) were acquired at six (for the wild-type) or five (for the others) Cl^- concentrations. These data sets were fitted independently with 4 exponential equations as described in MATERIALS AND METHODS. The results of the fitting analysis are summarized in Fig. 4. The panels in the upper row show the Cl^- dependencies of four time constants for the decay of the P_1-P_4 states. In all three samples, τ_3 and τ_4 depend on the Cl^- concentration. τ_3 is commonly accelerated by the increase in Cl^- concentration, but

the changes in τ_4 are different between the wild-type *p*hR and others. With increasing Cl^- concentration, τ_4 increases slightly for wild-type *p*hR but decreases for P240T/F250Y^{phR} and its complex with *p*HtrII$^{1-159}$.

In the panels from the second to bottom rows, the spectra of P_1-P_4 are depicted together with the spectrum of the unphotolyzed state (P_0). In all three samples, the spectra of P_1 and P_2 were almost the same and were independent of the Cl^- concentration. Those absorption maximum were about 520 nm, and so these states are assigned to the L_1- and L_2-intermediates, respectively. A significant difference among the three samples was observed in the P_3 state. The P_3 spectra of the wild-type have two peaks, implying a contribution from two physically defined intermediates in the equilibrium. This was confirmed by the global fitting of P_3 spectra. As shown in Fig. 5 A, the P_3 spectra were simulated well employing the sum of the skewed Gaussian functions. One component has an absorption maximum at around 610 nm. Judging from the absorption, this is the O-intermediate. Another

having a λ_{max} of ~ 510 nm is tentatively called the X-intermediate. It is noted that Chizhov and Engelhard also reported the existence of an intermediate having a λ_{max} similar to that of X and named it the N-intermediate (25). The obtained spectra of X- and O-intermediates are plotted in Fig. 5 B. With the increasing Cl^- concentration, a considerable shift in the equilibrium occurs from the O- to the X-intermediate. As shown in Fig. 4, the P_3 of P240T/F250Y^{phR} also appears to consist of X- and O-intermediates, but the shift in the equilibrium from the O- to X-intermediate occurs moderately. For the P_3 of the P240T/F250Y^{phR}-*p*HtrII$^{1-159}$ complex, the shift from O- to the X-intermediate was not observed even at 4.0 M Cl^- concentration. This disappearance of the X-intermediate is a notable difference from the Cl^--transporting photocycles of the wild-type and the double mutant. The Cl^--not-transporting photocycle of the complex may lack the X-intermediate itself.

The P_4 spectra of both the wild-type and P240T/F250Y^{phR} are almost the same as that of their unphotolyzed state (P_0).

Thus, these P_4 states consist mainly of the *p*hR'-intermediate, which might be a precursor of the original unphotolyzed state. On the other hand, the P_4 state of the P240T/F250Y^{phR}-*p*HtrII$^{1-159}$ complex had spectra slightly different from the P_0 state. This difference becomes evident at low Cl^- concentrations and causes the prolonged decay observed at 650 nm as shown in Fig. 3. Figure 6 shows the absorption differences between the P_4 and P_0 states (P_4-P_0). The absorption difference is evident for the complex (panel C). The difference becomes small as the Cl^- concentration increases. Moreover, small but similar absorption differences are also seen for the wild-type and the double mutant (panels A and B). These differences may originate in a slight contribution of a red-shifted intermediate other than the *p*hR'-intermediate.

DISCUSSION

The present paper obtained the following results: The first is that the interaction of P240T/F250Y^{phR} with *p*HtrII blocked the net Cl^- transport. Complete blocking was not obtained,

which may be due to a relatively weak binding between these components. The second is that the X-intermediate constituting P_3 was not seen during the photocycle of the complex between P240T/F250Y^{phR} and *p*HtrII$^{1-159}$, and the amount of this intermediate of P240T/F250Y^{phR} alone was smaller than that of the wild-type *p*hR (compare P_3 components in Fig. 4). The photocycle rates of the wild-type *p*hR, the double mutant and the complex were not significantly changed (see Fig. 3 and the top panels of Fig. 4). Comparison of the magnitude of the photocurrents (Fig. 2) with the amounts of the X-intermediate constituting P_3 (Fig. 4) suggests that there is a rough correlation between these two factors.

For the complex, there is a direct correlation between the disappearances of Cl^--pumping activity and the X-intermediate. These observations imply that the complex undergoes a photocycle lacking the X-intermediate whose formation is important for the Cl^- transport. For the double mutant alone, both the pumping activity and the amount of X-intermediate in P_3 were smaller than those of the wild-type.

In the case of the double mutant alone, thus, some extent of the excited molecules may undergo the Cl^--not-transporting photocycle as does the complex. The remaining molecules may undergo the Cl^--transporting photocycle. The co-existence of two photocycles appears consistent with the results for the double mutant alone. At present, however, we cannot explain the mechanism by which the double mutations cause the heterogeneity in the photocycle.

For the wild-type and the double mutant, the equilibrium between X- and O-intermediates in the P_3 states were shifted by the Cl^- concentration. The photo-current measurements shown in Fig. 2 were performed at a Cl^- concentration of about 100 mM. At such a low Cl^- concentration, the spectra of the P_3 states of the wild-type and the double mutant are dominated by the O-intermediate as is the P_3 state of the complex. For the wild-type and the double mutant, however, this does not mean that their Cl^-—pumping photocycles also lack the X-intermediate at the low Cl^- concentration. At the P_3 state of the Cl^-—pumping photocycle, the X- and O-intermediates are

considered to form the equilibrium quickly compared with the transition between the P_i states. The shift in the equilibrium toward the O-intermediate makes the X-intermediate unremarkable. However, the O-intermediate should still form the fast equilibrium with the X-intermediate even at the low Cl^- concentration.

The shift in the equilibrium in the P_3 state due to the Cl^- concentration means that this equilibrium should accompany the release and uptake of Cl^- between the protein and the external medium. For the wild-type *p*hR, Váró et al. (33) and Chizhov and Engelhard (25) also described a fast equilibrium between the anion-bound (X-intermediate) and the anion-free (O-intermediate) state. Due to the increase in the Cl^- concentration, the equilibrium shifts from the O- to the X-intermediate. This suggests that the O-intermediate is a Cl^--free state, which is very credible from its λ_{max}. The formation of this intermediate is thus associated with the Cl^- release, probably to the cytoplasmic (CP) space. This is

consistent with the conclusion drawn by other previous investigators (34-38).

Therefore, before the O-intermediate, an intermediate having bound Cl^- in the CP channel should exist. Previous reports (21,39,40) proposed that the binding site in the CP channel is Thr-203 for *s*hR and Thr-218 for *p*hR. If the Cl^- binding site in the CP channel is only this position (39,40), only one intermediate having Cl^- in the CP binding site should exist and the candidate may be either X or $P_2(L_2)$.

As for the reaction sequence from the P_2 to P_4 states of the wild-type *p*hR, there are 4 possible models as shown in Fig. 7. The absorption differences between the P_4 and P_0 state (shown in Fig. 6) imply that the P_4 state includes not only *p*hR' but also a small contribution from a red-shifted intermediate. Because a component whose λ_{max} is located at a longer wavelength than that of the original pigment is only the O-intermediate, the red-shifted component of P_4 may be the O-intermediate. It does not seem that the spectrum of P_4 is contributed from a component having a shorter wavelength such

as the X-intermediate. From these observations, we may rule out both models C and D. Thus, the *p*hR'-intermediate may be formed by the decay of the O-intermediate. During the O → phR' transition, Cl^- may enter into the binding site in the extracellular (EC) channel, because *p*hR' has almost the same photochemical properties of unphotolyzed *p*hR having only one Cl^- in the EC channel; the crystal structure of *s*hR (halorhodopsin from *H. salinarum*) shows that the unphotolyzed state has only one Cl^- in the EC channel (39).

According to the model B, the $P_2(L_2)$-intermediate should have Cl^- in the CP binding site, and during the $P_2(L_2)$ → O transition, Cl^- should be released. This implies no definite role of the X-intermediate, which is contradictory to the present observation that the intermediate of X is very important for the Cl^- transport. Therefore, model A is considered to be the most probable, and we assume the Cl^- movement to be as shown in Fig. 8.

The dependences of the X and O amounts on Cl^- concentration (shown in Fig. 5 A) are accountable by the above

scheme. When we adopt this scheme, the Cl^- entry from EC space may drive the decay of the O-intermediate, which pushes the $X \rightarrow O$ transition and results in Cl^- release into the CP space. Thus, the high concentration of Cl^- in the environment may prompt the Cl^- transport. A mechanism for the fast equilibrium between the X-intermediate (Cl^--binding in CP channel) and the O-intermediate (Cl^--free) is awaited in a further important study.

What is the physical identity of the X-intermediate? There are two possibilities: one is that X is distinct from L_2 while the other is that X is L_2. According to the first possibility, the X-intermediate should have one Cl^- in the CP channel, and the L_2 state may have Cl^- in the EC channel, probably near the Schiff base and Arg123 (Arg108 of *s*hR) provided that the Cl^- binding site in the CP channel is the only one (39,40). Because the Cl^- movement is confined within the molecule, τ_2 does not show the Cl^- dependence as was observed. Based on these considerations, X-intermediate is most probably assigned to the N-intermediate proposed previously.

Muneyuki *et al*. (41) and Ludmann *et al*. (38) described that the electrogenetic steps were the formation and decay of the N-intermediate, which is consistent with the present scheme.

Next let us consider the second possibility that X is L_2. The maximum wavelength of absorption of the X-intermediate (~510 nm) may be favorable for this. If we adopt this assumption, Cl^- might pass through the Schiff base region from the EC to the CP channel during the L_1 to L_2 transition. This may be contradictory to the conclusion drawn by Muneyuki *et al*. (41) and Ludmann *et al*. (38) mentioned above. When the possible molecular events are considered as below, this assumption leads to a somewhat more complicated story than the first assumption that X is N. However, this possibility that X is L_2 cannot be completely ruled out at present (42). To solve the question regarding the timing of the Cl^- movement from the EC to the CP channel is one of the key points in solving the physical identification of the X-intermediate as well as the Cl^- pumping mechanism.

Regardless of the physical identity of X, the experimental evidence obtained is that the transducer binding prevents the formation of X while the O-intermediate is observable. Note that at the X-intermediate, Cl^- is present at the CP binding site while the O-intermediate does not contain Cl^-. Because Cl^- resides at the EC binding site in unphotolyzed *p*hR, Cl^- should circulate within the EC channel under the transducer binding condition, resulting in the cessation of electrical current. A cartoon is illustrated in Fig. 9, which shows the possible mechanism of the blocking. The Cl^- binding site in CP is Thr218 of *p*hR (21) that is located at the F-helix. The transducer interacts with *p*hR at the F- and G-helices. This strongly suggests the necessity of the conformational change in the F – G helices at the X-intermediate such as the opening of the F-helix occurs in bR at the late M- and N-intermediate (43-48).

If X is L_2, the story may become somewhat complicated: Cl^- passes from EC to the CP channel at the L_1 to L_2 transition and should return to the EC channel again in the case of complex.

The dead end of the Cl^- exit at the CP channel due to a so-called cytoplasmic closure by the transducer and the flip of the N-H dipole (13-*cis* to all-*trans* retinal) at the L_2 to O transition might possibly exert a driving force for this return of Cl^-, but this does not seem to occur. Hence, the assumption that X is N (not L_2) may provide a more straightforward explanation.

The transducer binding occurs at the EC half of the archaeal rhodopsins and the mutated 240^{th} and 250^{th} positions are located at the F-G loop (positioned at the EC space) and the middle of the G-helix, respectively. The intermediate of *p*hR' may be a state where Cl^- is located at the EC channel different from that of the unphotolyzed *p*hR. The change in the amino acid residues at the 240^{th} and 250^{th} positions may alter the Cl^--locating position in *p*hR', which may give rise to the change in the equilibrium between *p*hR'- and O-intermediate in the P_4 state and the Cl^- dependence of τ_4 from those of the wild-type.

REFERENCES

1. Matsuno-Yagi, A. and Y. Mukohata (1980) ATP synthesis linked to light-dependent proton uptake in a red mutant strain of *Halobacterium* lacking bacteriorhodopsin, *Arch. Biochem. Biophys.* **199**, 297-303.

2. Váró, G. (2000) Analogy between halorhodopsin and bacteriorhodopsin, *Biochim. Biophys. Acta* **1460**, 220-229.

3. Essen, L. O. (2002) Halorhodopsin: Light-driven ion pumping made simple?, *Curr. Opin. Struct. Biol.* **12**, 516-522.

4. Lanyi, J.K. and H. Luecke (2001) Bacteriorhodopsin, *Curr. Opin. Struct. Biol.* **11**, 415-419.

5. Haupts, U., J. Tittor and D. Oesterhelt (1999) Closing in on bacteriorhodopsin: Progress in understanding the molecule, *Annu. Rev. Biophys. Biomol. Struct.* **28**, 367-399.

6. Spudich, J.L. and R.A. Bogomolni (1984) Mechanism of color discrimination by a bacterial sensory rhodopsin, *Nature* **312**, 509-513.

7. Hazemoto, N., N. Kamo, Y. Terayama, Y. Kobatake and M. Tsuda (1983) Photochemistry of two rhodopsin-like pigments in bacteriorhodopsin-free mutant of *Halobacterium halobium*, *Biophys. J.* **44**, 59-64.

8. Takahashi, T., H. Tomioka, N. Kamo and Y. Kobatake (1985) A photosystem other than PS370 also mediates the negative phototaxis of *Halobacterium halobium, FEMS Microbiol. Lett.* **28**, 161-164.

9. Tomioka, H., T. Takahashi, N. Kamo and Y. Kobatake (1986) Flash spectrophotometric identification of a 4^{th} rhodopsin-like pigment in *halobacterium halobium*, *Biochem. Biophys. Res. Commun.* **139**, 389-395.

10. Kamo, N., K. Shimono, M. Iwamoto and Y. Sudo (2001) Photochemistry and photoinduced proton-transfer by *pharaonis* phoborhodopsin, *Biochemistry (Mosc)* **66**, 1277-1282.

11. Luecke, H., B. Schobert, J.K. Lanyi, E.N. Spudich and J.L. Spudich (2001) Crystal structure of sensory rhodopsin II at 2.4 angstroms: Insights into color tuning and transducer interaction, *Science* **293**, 1499-1503.

12. Hoff, W.D., K.H. Jung and J.L. Spudich (1997) Molecular mechanism of photosignaling by archaeal sensory rhodopsins, *Annu. Rev. Biophys. Biomol. Struct.* **26**, 223–258.

13. Sudo, Y., H. Kandori and N. Kamo (2004) Molecular mechanism of protein-protein interaction of *pharaonis* phoborhodopsin/transducer and photo-signal transfer reaction by the complex, *Recent Res. Devel. Biophys.* **3**, 1–16.

14. Zhang, X.N., J. Zhu and J.L. Spudich (1999) The specificity of interaction of archaeal transducers with their cognate sensory rhodopsins is determined by their transmembrane helices, *Proc. Natl Acad. Sci. USA* **96**, 857–862.

15. Rudolph, J and D. Oesterhelt (1996) Deletion analysis of the che operon in the archaeon *Halobacterium salinarium*, *J. Mol. Biol.* **258**, 548–554.

16. Rudolph, J., B. Nordmann, K.F. Storch, H. Gruenberg, K. Rodewald and D. Oesterhelt (1996) A family of halobacterial transducer proteins, *FEMS Microbiol. Lett.* **139**, 161–168.

17. Falke, J.J., R.B. Bass, S.L. Butler, S.A. Chervitz and M.A. Danielson (1997) The two-component signaling pathway of bacterial chemotaxis: a molecular view of signal transduction by receptors, kinases, and adaptation enzymes, *Annu. Rev. Cell Dev. Biol.* **13**, 457–512.

18. Gordeliy V.I., J. Labahn, R. Moukhametzianov, R. Efremov , J. Granzin, R. Schlesinger, G. Büldt, T. Savopol, A.J. Scheidig, J.P. Klare and M. Engelhard (2002) Molecular basis of transmembrane signalling by sensory rhodopsin II-transducer complex, *Nature* **419**, 484–487.

19. Sudo, Y., M. Yamabi, S. Kato, C. Hasegawa, M. Iwamoto, K. Shimono and N. Kamo (2006) Importance of specific hydrogen bonds of archaeal rhodopsins for the binding to the transducer protein. *J. Mol. Biol.* **357**, 1274-1282.

20. Sudo, Y., M. Iwamoto, K. Shimono and N. Kamo (2001) *Pharaonis* phoborhodopsin binds to its cognate truncated transducer even in the presence of a detergent with a 1:1 stoichiometry, *Photochem. Photobiol.* **74**, 489-494.

21. Sato, M., M. Kubo, T. Aizawa, N. Kamo, T. Kikukawa, K. Nitta and M. Demura (2005) Role of putative anion-binding

sites in cytoplasmic and extracellular channels of *Natronomonas pharaonis* halorhodopsin, *Biochemistry* **44**, 4775-4784.

22. Sudo, Y., M. Yamabi, M. Iwamoto, K. Shimono and N. Kamo (2003) Interaction of *Natronomonas pharaonis* phoborhodopsin (sensory rhodopsin II) with its cognate transducer probed by increase in the thermal stability, *Photochem. Photobiol.* **78**, 511-516.

23. Miyauchi, S., E. Gopal, Y.J. Fei and V. Ganapathy (2004) Functional identification of SLC5A8, a tumor suppressor down-regulated in colon cancer, as a Na(+)-coupled transporter for short-chain fatty acids, *J. Biol. Chem.* **279**, 13293-13296.

24. Chizhov, I., D.S. Chernavskii, M. Engelhard, K.H. Mueller, B.V. Zubov and B. Hess (1996) Spectrally silent transitions in the bacteriorhodopsin photocycle, *Biophys. J.* **71**,

2329–2345.

25. Chizhov, I. and M. Engelhard (2001) Temperature and halide dependence of the photocycle of halorhodopsin from *Natronobacterium pharaonis*, *Biophys. J.* **81**, 1600–1612.

26. Nagel, G., B. Möckel, G. Büldt and E. Bamberg (1995) Functional expression of bacteriorhodopsin in oocytes allows direct measurement of voltage dependence of light induced H^+ pumping, *FEBS Lett.* **377**, 263–266.

27. Nagel, G., D. Ollig, M. Fuhrmann, S. Kateriya, A.M. Musti, E. Bamberg and P. Hegemann (2002) Channelrhodopsin-1: A light-gated proton channel in green algae, *Science* **296**, 2395-2398.

28. Schmies, G., B. Lüttenberg, I. Chizhov, M. Engelhard, A. Becker and E. Bamberg (2000) Sensory rhodopsin II from the

haloalkaliphilic *Natronobacterium pharaonis*: Light-activated proton transfer reactions, *Biophys. J.* **78**, 967-976.

29. Schmies, G., M. Engelhard, P. G. Wood, G. Nagel and E. Bamberg (2001) Electrophysiological characterization of specific interactions between bacterial sensory rhodopsins and their transducers, *Proc. Natl. Acad. Sci. USA* **98**, 1555-1559.

30. Hippler-Mreyen, S., J.P. Klare, A.A. Wegener, R. Seidel, C. Herrmann, G. Schmies, G. Nagel, E. Bamberg and M. Engelhard (2003) Probing the sensory rhodopsin II binding domain of its cognate transducer by calorimetry and electrophysiology, *J. Mol. Biol.* **330**, 1203-1213.

31. Bogomolni, R.A., W. Stoeckenius, I. Szundi, E. Perozo, K.D. Olson and J.L. Spudich (1994) Removal of transducer HtrI allows electrogenic proton translocation by sensory rhodopsin

I, *Proc. Natl. Acad. Sci. USA* **91**, 10188-10192.

32. Sudo, Y, M. Iwamoto, K. Shimono, M. Sumi and N. Kamo (2001) Photo-induced proton transport of *pharaonis* phoborhodopsin (sensory rhodopsin II) is ceased by association with the transducer, *Biophys. J.* **80**, 916-922.

33. Váró, G., L.S. Brown, J. Sasaki, H. Kandori, A. Maeda, R. Needleman and J.K. Lanyi (1995) Light-driven chloride ion transport by halorhodopsin from *Natronobacterium pharaonis.* 1. the photochemical cycle, *Biochemistry* **34**, 14490-14499.

34. Sato, M., T. Kanamori, N. Kamo, M. Demura and K. Nitta (2002) Stopped-flow analysis on anion binding to blue-form halorhodopsin from *Natronobacterium pharaonis*: comparison with the anion-uptake process during the photocycle, *Biochemistry* **41**, 2452-2458.

35. Zimanyi, L. and J.K. Lanyi (1989) Transient spectroscopy

of bacterial rhodopsins with an optical multichannel analyzer. 2. Effects of anions on the halorhodopsin photocycle, *Biochemistry* **28**, 5172-5179.

36. Ames, J.B., J. Raap, J. Lugtenburg and R.A. Mathies (1992) Resonance Raman study of halorhodopsin photocycle kinetics, chromophore structure, and chloride-pumping mechanism, *Biochemistry* **31**, 12546-12554.

37. Váró, G., R. Needleman and J.K. Lanyi (1995) Light-driven chloride ion transport by halorhodopsin from *Natronobacterium pharaonis.* 2. chloride release and uptake, protein conformation change, and thermodynamics, *Biochemistry* **34**, 14500-14507.

38. Ludmann, K., G. Ibron, J.K. Lanyi and G. Váró (2000) Charge motions during the photocycle of *pharaonis* halorhodopsin, *Biophys. J.* **78**, 959-966.

39. Kolbe, M., H. Besir, L.O. Essen and D. Oesterhelt (2000) Structure of the light-driven chloride pump halorhodopsin at 1.8 Å resolution, *Science* **288**, 1390-1396.

40. Rüdiger, M. and D. Oesterhelt (1997) Specific arginine and threonine residues control anion binding and transport in the light driven chloride pump halorhodopsin, *EMBO J.* **16**, 3813-3821.

41. Muneyuki, E., C. Shibazaki, H. Ohtani, D. Okuno, M. Asaumi and T. Mogi (1999) Time-resolved measurements of photovoltage generation by bacteriorhodopsin and halorhodopsin adsorbed on a thin polymer film, *J. Biochem. (Tokyo)* **125**, 270-276.

42. Shibata, M., N. Muneda, T. Sasaki, K. Shimono, N. Kamo, M. Demura and H. Kandori (2005) Hydrogen-bonding alterations of the protonated Schiff base and water molecule in the chloride pump of *Natronobacterium pharaonis*, *Biochemistry* **44**, 12279-12286.

43. Subramaniam, S. and R. Henderson (2000) Molecular mechanism of vectorial proton translocation by bacteriorhodopsin, *Nature* **406**, 653-657.

44. Sass, H.J., G. Buldt, R. Gessenich, D. Hehn, D. Neff, R. Schlesinger, J. Berendzen and P. Ormos (2000) Structural alterations for proton translocation in the M state of wild-type bacteriorhodopsin, *Nature* **406**, 649-653.

45. Vonck, J. (2000) Structure of the bacteriorhodopsin mutant F219L N intermediate revealed by electron crystallography, *EMBO J.* **19**, 2152-2160.

46. Radzwill, N., K. Gerwert and H.J. Steinhoff (2001) Time-resolved detection of transient movement of helices F and G in doubly spin-labeled bacteriorhodopsin, *Biophys. J.* **80**, 2856-2866.

47. Oka, T., N. Yagi, F. Tokunaga and M. Kataoka (2002) Time-resolved X-ray diffraction reveals movement of F helix of D96N bacteriorhodopsin during M-MN transition at neutral pH, *Biophys. J.* **82**, 2610-2616.

48. Klare, J.P., E. Bordignon, M. Engelhard and H.J. Steinhoff (2004) Sensory rhodopsin II and bacteriorhodopsin: Light activated helix F movement, *Photochem. Photobiol. Sci.* **3**, 543-547.

FIGURE LEGENDS

Figure 1. Denaturation kinetics of the *p*hR mutants. The *p*hR mutants were incubated at high temperatures in the absence or presence of *p*HtrII$^{1-159}$, and the residual amounts of the mutants were determined by their absorption at 578 nm. The incubation temperatures were 70°C for P240T^{phR} (A), 60°C for F250Y^{phR} (B) and P240T/F250Y^{phR} (C). The concentrations of these mutants were 10 μM, and the mole ratios of the mutants and *p*HtrII$^{1-159}$ are denoted in the figures.

Figure 2. The photo-induced currents *via* *p*hR and P240T/F250Y^{phR} expressed in *Xenopus* oocytes, and the Western blot analysis for the protein expressions. (A) The photo-induced current *via* wild-type *p*hR and its P240T/F250Y^{phR} mutant. The expression amount of the mutant was about half that of the wild-type (lanes 1 and 2 in panel (C)). (B) The change in the photo-induced current *via* the P240T/F250Y^{phR} mutant with the increase in the expression amount of *p*HtrII$^{1-159}$.

In the oocytes used, the expression amounts of P240T/F250Y^{phR} were almost the same. Here, the photo-induced current was plotted against the mole ratio of expressed P240T/F250Y^{phR} and *p*HtrII$^{1-159}$ evaluated by the corresponding Western blots (lanes 3-6 in panel (C)). Through the measurements in panels (A) and (B), the membrane potential was clamped at -50 mV. Each bar represents the mean ± SD for between 9-11 oocytes. (C) The Western blot analysis of the membrane fractions of the oocytes using the anti-His-Tag monoclonal antibody. The upper bands correspond with wild-type *p*hR or P240T/F250Y^{phR}, and the lower bands correspond with *p*HtrII$^{1-159}$. Lanes 1 and 2: the oocytes were injected with 50 ng of cRNAs of wild-type *p*hR and P240T/F250Y^{phR}, respectively. Lanes 3-6: the cRNA amounts of P240T/F250Y^{phR} were kept at 30 ng, while those of *p*HtrII$^{1-159}$ were varied as 0, 2.5, 5 and 10 ng, respectively.

Figure 3. Flash-induced transient absorption changes at typical wavelengths. Buffer solutions were 10 mM Mops at pH

7.0 containing 0.1% DDM and 0.2 M (upper row) or 4.0 M (lower row) NaCl. All measurements were performed at 20°C.

Figure 4. Results of the global fitting of the flash-photolysis data. The top row represents the dependence of the time constants of the P_1-P_4 states on the Cl^- concentration. In the panels from the second to bottom rows, the absolute spectra of photochemically defined states P_1-P_4 at six Cl^- concentrations between 0.2 and 4.0 M are depicted with the spectrum of the unphotolyzed state P_0 (gray solid line). At the P_3 and P_4 states, notable differences were seen in their absolute spectra, and so the numbers are depicted in the panels to denote the Cl^- concentration as: 1, 0.2 M; 2, 0.4 M; 3, 0.6 M; 4, 1.0 M; 5, 2.0 M; 6, 4.0 M. The spectrum of P_0 is expressed by the sum of two skewed Gaussian functions whose parameters were λ_{max}=575.1 nm, A_{max}=1.0, ρ=1.58 and $\Delta\nu$=3254.3 cm^{-1} for the main absorption band and λ_{max}=405.6 nm, A_{max}=0.09, ρ=1.24 and $\Delta\nu$=1693.1 cm^{-1} for the β-band (for details, see MATERIALS AND METHODS). The absorption spectra were identical between wild-type *p*hR and P240T/F250Y^{phR}. These

spectra did not change throughout all the conditions we used.

Figure 5. Multi-Gaussian fit of the P_3 state of wild-type *p*hR. (A) The absolute spectra of the P_3 state at various Cl^- concentrations (○) were fitted simultaneously by the sum of the three skewed Gaussian functions expressing the X- and O-intermediates and their β-bands. Here, we assumed that their β-bands were identical with that of the unphotolyzed state (P_0). The fitting results are shown in smooth lines. The numbers depicted in the figure denote the Cl^- concentrations as shown in Fig. 4. The inset shows the change in the fractions of X- and O-intermediates under various Cl^- concentrations. (B) Spectra of X- and O-intermediates determined. For comparison, the spectra of P_0 (gray solid line), and the P_2 and P_3 states are also plotted. The parameters of the skewed Gaussian functions are λ_{max}=507.1 nm, A_{max}=0.56, ρ=1.64 and $\Delta\nu$=2688.1 cm^{-1} for the main band of the X-intermediate, and λ_{max}=604.9 nm, A_{max}=1.05, ρ=1.47 and $\Delta\nu$=3198.5 cm^{-1} for that of the O-intermediate, respectively.

Figure 6. Absorption differences between the P_4 and P_0 states of (A) wild-type *p*hR, (B) P240T/F250Y^{phR} and (C) its complex with *p*HtrII$^{1-159}$. The differences in the relative absorbances, P_4-P_0, are plotted. The Cl^- concentrations are denoted in the figures.

Figure 7. Possible models for the reaction sequence from the P_2 to P_4 states of the wild-type *p*hR.

Figure 8. Plausible reaction sequence from the P_2 to P_4 states of the wild-type *p*hR. At the P_3 state, the X- and O-intermediates are in the equilibrium accompanying the release and uptake of Cl^- at the CP side. The reuptake of Cl^- at the EC side proceeds during the O $\rightarrow$ *p*hR' transition. The contribution of the O-intermediate to the P_4 state is very small, and so the P_4 state is represented here by only the *p*hR'-intermediate.

Figure 9. The model of the external Cl^- circulation during the photocycle of the P240T/F250Y^{phR}-*p*HtrII$^{1-159}$ complex. The upper and lower paths express the photocycles of the wild-type *p*hR and the P240T/F250Y^{phR}-*p*HtrII$^{1-159}$ complex, respectively. Here, we assume that the formation of the X-intermediate appearing in the normal photocycle accompanies the Cl^- displacement from the Schiff base to its binding site in the CP channel. The binding with *p*HtrII$^{1-159}$ disturbs the CP opening of P240T/F250Y^{phR}, which results in the blocking of the Cl^- displacement to the CP channel. Consequently, the release and reuptake of Cl^- occur at only the EC side during the formation and decay of the O-intermediate. The *p*hR'-intermediate of the complex may take a slightly different Cl^- configuration from that of the normal photocycle (for details see text).

Fig. 1

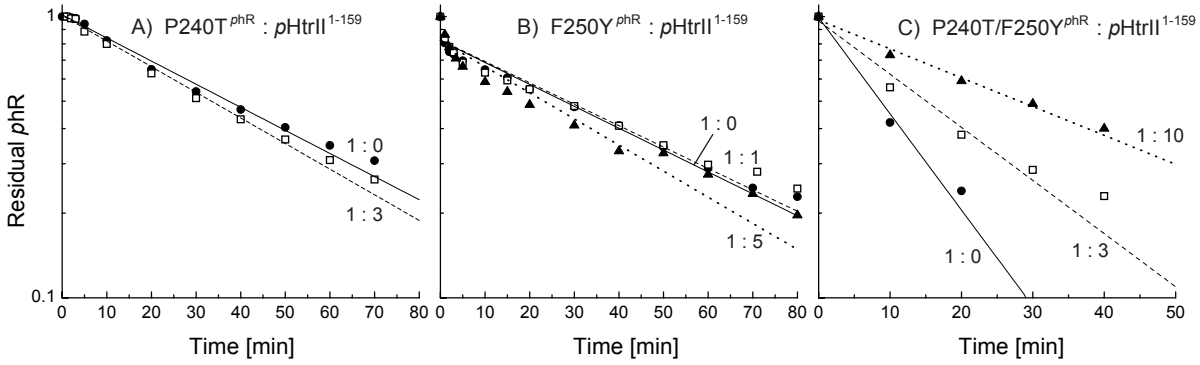
A) P240T phR : pHtrII 1-159
B) F250Y phR : pHtrII 1-159
C) P240T/F250Y phR : pHtrII 1-159
Residual phR
Time [min]
1 : 0
1 : 3
1 : 1
1 : 5
1 : 10

Fig. 2

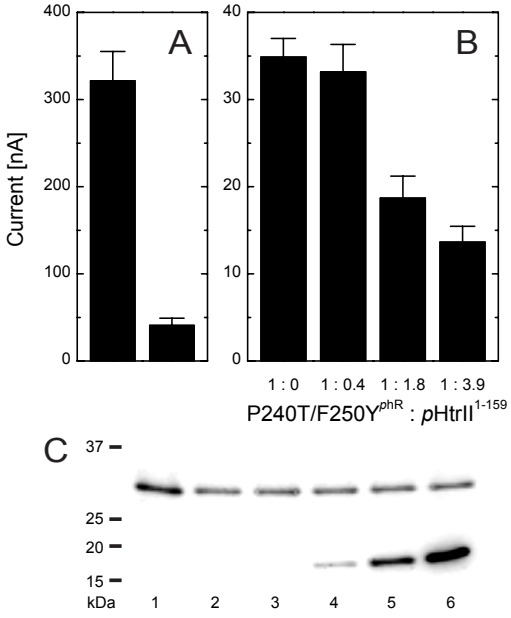
A
B
C
Current [nA]
400
300
200
100
0
40
30
20
10
0
1 : 0
1 : 0.4
1 : 1.8
1 : 3.9
P240T/F250Y^phR : pHtrII^1-159
37
25
20
15
kDa
1
2
3
4
5
6

Fig. 3

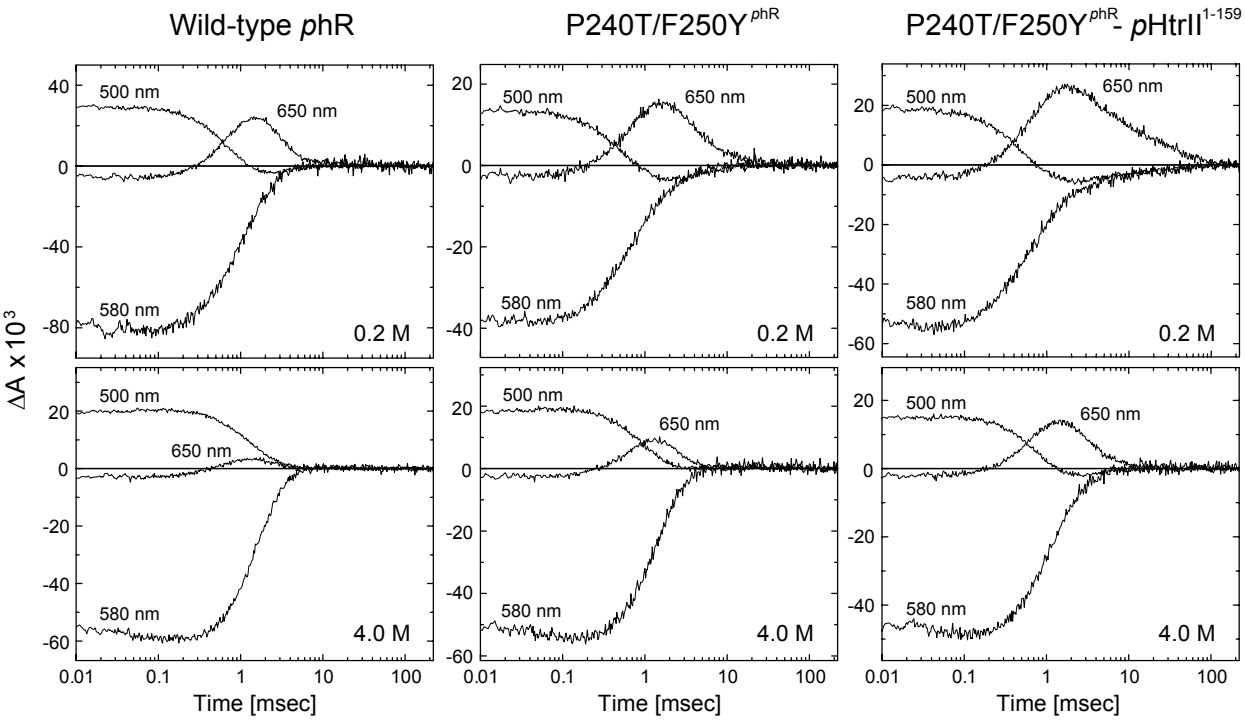
Wild-type *p*hR
P240T/F250Y*p*hR
P240T/F250Y*p*hR- *p*HtrII1-159
ΔA x 10^3
500 nm
650 nm
580 nm
0.2 M
4.0 M
Time [msec]
0.01
0.1
1
10
100

Fig. 4

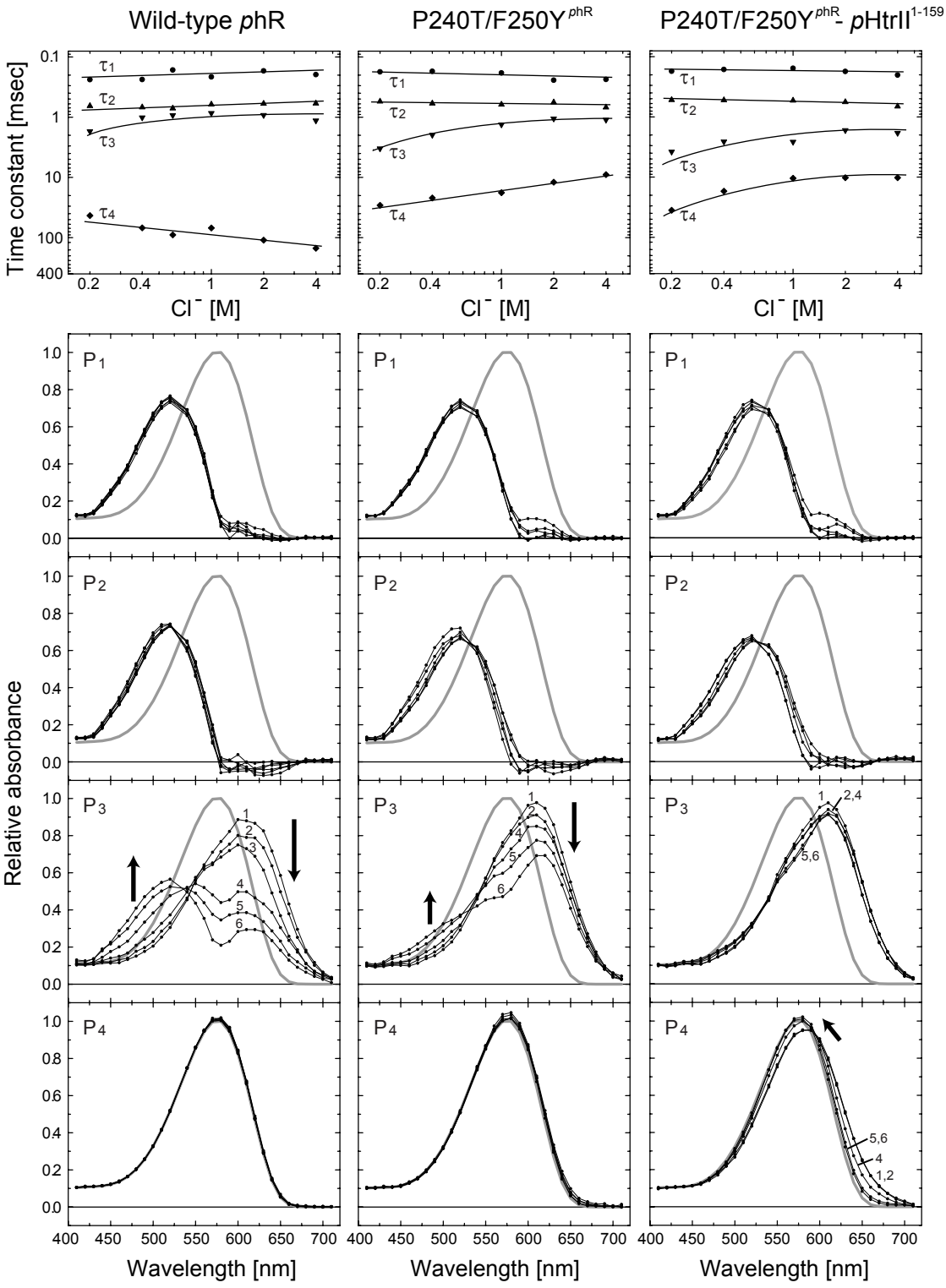
Wild-type phR
P240T/F250Y phR
P240T/F250Y phR- pHtrII 1-159
Time constant [msec]
τ1
τ2
τ3
τ4
Cl⁻ [M]
P1
P2
P3
P4
Relative absorbance
Wavelength [nm]

Fig. 5

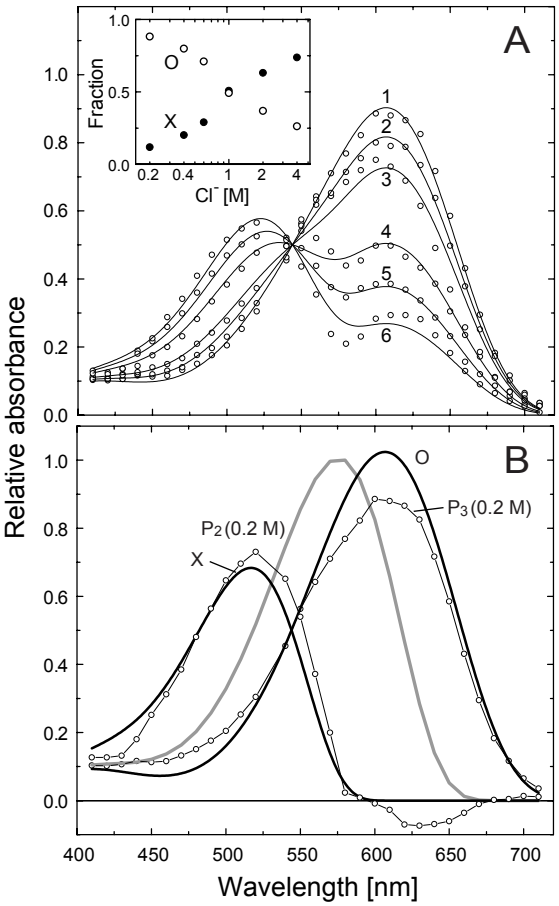
A
B
Fraction
O
X
Cl⁻ [M]
1
2
3
4
5
6
Relative absorbance
P2(0.2 M)
P3(0.2 M)
Wavelength [nm]

Fig. 6

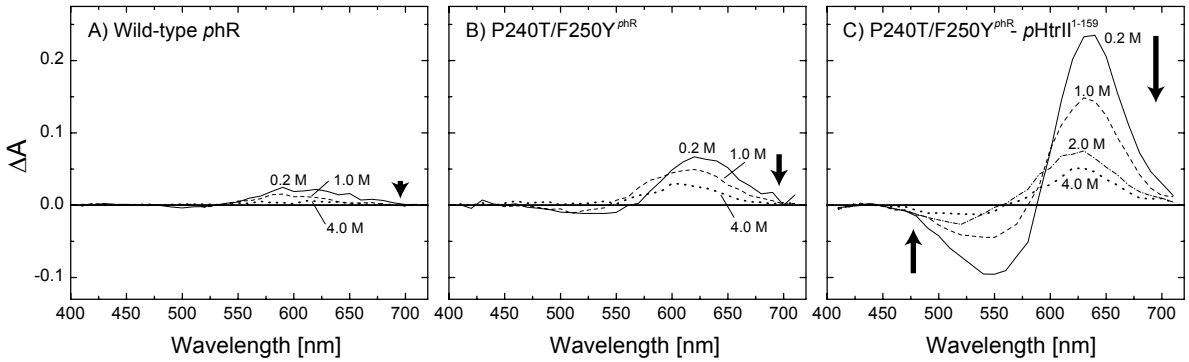
A) Wild-type *p*hR
B) P240T/F250Y^{phR}
C) P240T/F250Y^{phR} - *p*HtrII$^{1-159}$
ΔA
0.2
0.1
0.0
-0.1
0.2 M
1.0 M
2.0 M
4.0 M
400
450
500
550
600
650
700
Wavelength [nm]

Fig. 7

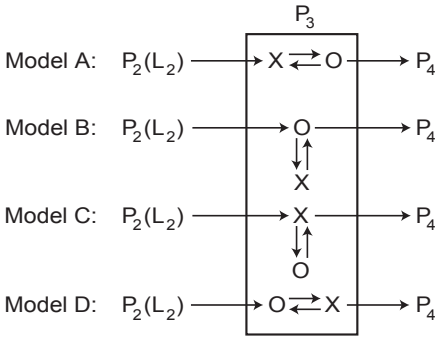
P3
Model A:
P2(L2)
X
O
P4
Model B:
P2(L2)
O
X
P4
Model C:
P2(L2)
X
O
P4
Model D:
P2(L2)
O
X
P4

Fig. 8

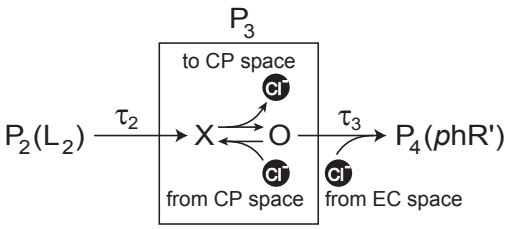
P3
to CP space
Cl-
P2(L2)
τ2
X
O
τ3
P4(phR')
Cl-
Cl-
from CP space
from EC space

Fig. 9

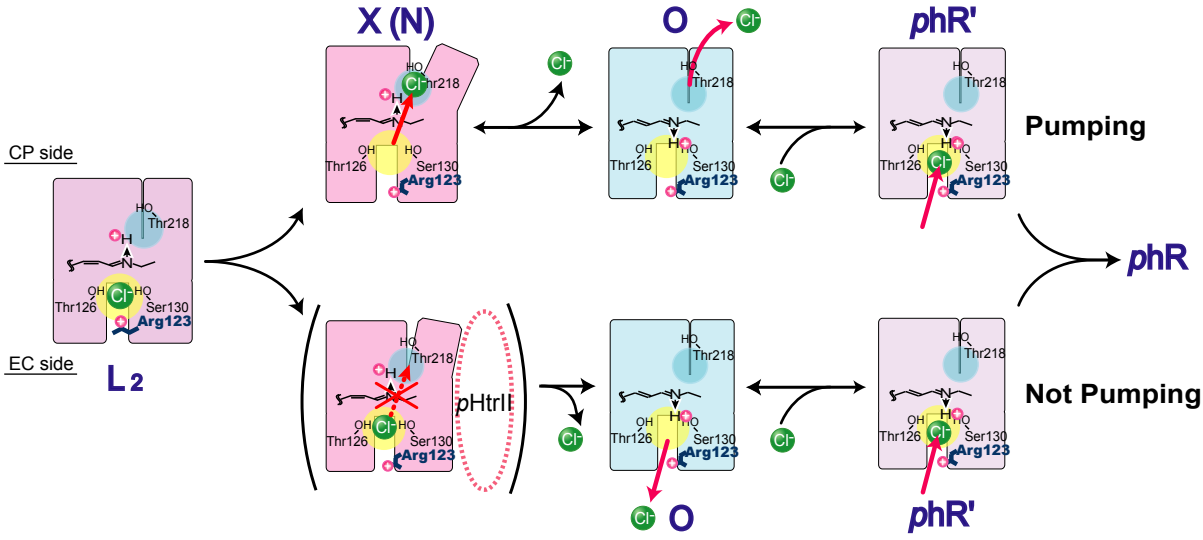
X (N)
O
phR'
Pumping
CP side
EC side
L2
Thr218
Thr126
Ser130
Arg123
pHtrII
phR
Not Pumping